Eur. Phys. J. E **33**, 149–163 (2010)
DOI 10.1140/epje/i2010-10611-6

THE EUROPEAN PHYSICAL JOURNAL E

Regular Article

Physical determinants of vascular network remodeling during tumor growth

M. Welter and H. Rieger[a]

Theoretical Physics, Saarland University, 66041 Saarbrücken, Germany

Received 11 February 2010
Published online: 6 July 2010 –

Abstract. The process in which a growing tumor transforms a hierarchically organized arterio-venous blood vessel network into a tumor specific vasculature is analyzed with a theoretical model. The physical determinants of this remodeling involve the morphological and hydrodynamic properties of the initial network, generation of new vessels (sprouting angiogenesis), vessel dilation (circumferential growth), vessel regression, tumor cell proliferation and death, and the interdependence of these processes via spatio-temporal changes of blood flow parameters, oxygen/nutrient supply and growth factor concentration fields. The emerging tumor vasculature is non-hierarchical, compartmentalized into well-characterized zones, displays a complex geometry with necrotic zones and "hot spots" of increased vascular density and blood flow of varying size, and transports drug injections efficiently. Implications for current theoretical views on tumor-induced angiogenesis are discussed.

1 Introduction

Tissues in living organisms need a persistent supply with oxygen and other nutrients provided by the vascular blood flow through the vessel network threading the tissue. Fast proliferating cells in a growing tumor have an increased oxygen/nutrient demand, for which reason tumors usually cannot grow beyond a size of 1-2 mm^3 without modifying the original vasculature. This modification, comprising a substantial increase of microvascular density in the growth zone of the tumor, is denoted as angiogenesis, the creation of new blood vessels from existing ones [1].

The emerging tumor vasculature is in many respects different from the hierarchically organized arterio-venous blood vessel network in normal tissues. The expected increase in microvascular density (MVD) is usually observed in the periphery of the tumor, whereas the morphology of the vasculature in the tumor center is characterized by decreased MVD, dilated vessels, and regions of necrotic tumor tissue [2–5]. The resulting tumor-specific capillary network is very heterogeneous, composed of dense and void regions, and has geometric properties different from normal arterio-venous or normal capillary networks.

Besides pro- and anti-angiogenic molecular factors, mechanical, hydrodynamical and collective processes must be involved in the process that transforms or remodels the original arterio-venous blood vessel network into a tumor-specific vasculature. In this paper we want, with the help of a theoretical model, to address the physical determinants of the dynamical evolution, final morphology and blood flow properties of a tumor blood vessel network. We hypothesize that co-option of existing vessels and vessel regression, besides angiogenic sprouting and vessel dilation, are essential processes that determine the geometric and hydrodynamic properties of the tumor vasculature.

The study of theoretical models of tumor growth has a long and multifaceted history (for recent reviews, see [6, 7] and references therein). Earlier work focusing on tumor-induced angiogenesis can roughly be divided into three categories: 1) continuum models without a proper representation of a blood vessel network and blood flow [8–12]; 2) hybrid models with a fixed vessel network geometry and a dynamically evolving tumor [13–15]; and 3) hybrid models with a fixed tumor (as a source of a diffusing growth factor) and a dynamically evolving tumor vasculature starting from a single parent vessel far away from the growth factor source [16–19].

The latter models are also denoted as vessel-ingrowth models since the whole tumor vasculature grows from outside towards the tumor surface. Subsequent work was still inspired by these vessel-in-growth models [20–24]: although in these studies the tumor also evolved dynamically, focusing on a detailed analysis of the interactions between tumor and host tissue, all new vessels started to grow from one or more parent vessels in a non-physiologically far distance from the tumor. The remodeling process that transforms the original arterio-venous vasculature of the host tissue into a tumor-specific vessel network has not been addressed with this Ansatz, which is the topic of the work that we present in this paper.

[a] e-mail: h.rieger@mx.uni-saarland.de

In recent work [25–27], see also [28], the issue of vascular remodeling in a growing tumor by the three basic mechanisms —angiogenic sprouting, vessel regression and dilation— was addressed in a model that comprised a regular capillary grid as initial vascular network. The compartmentalization of the tumor as well as other global features, like the time and radius dependences of average MVD, tumor cell density, vessel radius and blood flow characteristics, were predicted in good agreement with experimental data, but local characteristics, like a single hot spot in the center and a general bias in the flow direction, could be attributed to the special topology of the initial network. In this paper we consider a more realistic three-dimensional arterio-venous vascular network as initial vasculature and study the effect it has on the emerging tumor vasculature. It is based on a simplified two-dimensional model that was studied in [29].

In well-vascularized tissue the average inter-capillary distance is 50–100 μm, in highly vascularized tissue like brain even less (depending on the oxygen demand and the resulting diffusion length), implying the importance of the incorporation of the original vasculature into a model for tumor-induced angiogenesis. This vasculature is organized in a hierarchical way, in which an arterial and a venous tree are interdigitated by capillaries. Oxygen and other nutrients are distributed into the surrounding tissue by the lowest-level capillaries, the two trees representing their supply and drainage system. The MVD, given by the average inter-capillary distance, is homogeneous in one kind of tissue to provide a homogeneous oxygen and nutrient supply, but the two interdigitating hierarchical trees form a spatially very inhomogeneous blood vessel network. Consequently the vascular remodeling process in a growing tumor will also be spatially inhomogeneous: sprouting angiogenesis occurs mainly from capillaries and venules, higher-level arteries protected by a thick layer of pericytes are more stable and regress later or not at all, regression of higher level arteries has fatal consequences for the whole arterial sub-tree below it, newly formed vessels between arteries and veins could act as shunts redirecting huge amount of blood, etc.

With this background we want to analyze the transformation of the well-organized hierarchical structure of an arterio-venous vessel network when it is co-opted and remodeled by an aggressively growing tumor. We are interested in the geometrical characteristics of the emerging tumor vasculature and the potential mechanisms leading to spatial inhomogeneities or hot spots. And we will study the global blood flow patterns and the drug transport performance of the tumor vasculature. The paper is organized as follows: In the next section the model is defined, including the method to construct an arterio-venous initial network. Section 3 presents the results for global properties for a choice of parameters that is guided by experimental data for melanoma [4,5]. These results include a discussion of the emerging morphologies; radial distributions of vessel density, vessel radius, tumor density, flow rates, shear forces, etc., vessel statistics, parameter dependencies, spatial inhomogeneities, and drug flow. Section 4 concludes the paper with a summary of the main results and a discussion.

2 Model definition

An arterio-venous network serves as the initial vasculature for our model of remodeling by a growing tumor. Depending on the local oxygen concentration, tumor cells represent the sources of the diffusion determined growth factor (GF) concentration field, which triggers either the generation of tip cells for angiogenic sprouting from existing vessels outside or at the periphery of the tumor, or circumferential growth within the tumor (for potential molecular mechanisms for this switch in the angiogenic program within the tumor, see [30]). In contrast to vessel in-growth models as in [16], tip cells are not dominantly generated by branching of existing tip cells but by sprouting from vessels of the original network. Lateral inhibition leads to a minimum spatial distance in a vessel segment between individual tip cell generation events [31].

Tip cells migrate in the direction of a sufficiently large GF gradient (chemotaxis), otherwise randomly. The path they describe is supposed to be filled with stalk cells forming a lumen and finally, once the tip cell hits another vessel (anastomosis), a functional vessel carrying blood flow is formed. Due to the pre-existing vasculature, vessels typically migrate only 50–100 μm before the filopodia of the tip cell extending up to 20–30 μm into the surrounding tissue in all directions [32] touch another vessel. Therefore directional cues are not as important here as in pure vessel in-growth models. And tip cells migrate maximally 100–150 μm and in case they did not make successful contact with another vessel, they retreat [33].

Inside the tumor, vessels destabilize and regress (for the potential molecular determinants of this destabilization, see [2,3]). In our model an increasing contact time of vessels with tumor cells, implying an increasing residence time within the tumor, leads to a higher collapse probability of tumor vessels. The collapse probability is also correlated with the origin of the vessel (artery, vein or capillary) and the shear force exerted by the blood flow upon the vessel walls [34].

2.1 Configuration space

The model consists of a discrete representation of the vasculature and continuum models for a non-specific growth factor concentration g, oxygen concentration o and tumor-cell density c.

The vasculature can be described as a graph where edges represent vessel segments and nodes represent branching points, respectively. This graph is embedded in a regular cubic lattice with the lattice constant Δl, which means that the nodes are located at the lattice sites and edges are coincident with the lattice edges. Vessels and nodes are dynamically created and destroyed over time. In Addition they have attached biophysical properties which can also vary over time.

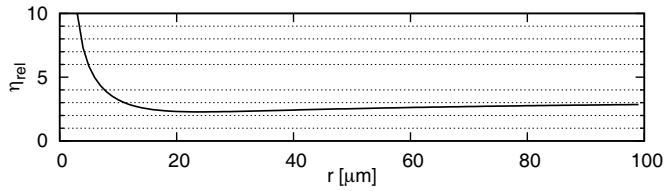

Fig. 1. Relative viscosity $\eta_{\rm rel}$ as a function of the vessel radius r. The actual viscosity is the viscosity of blood plasma $\eta = 4 \cdot 10^{-6}\,\mathrm{kPa\,s} \times \eta_{\rm rel}$. The shape of $\eta_{\rm rel}$ was obtained from a best fit of experimental *in vitro* data [37]. $\eta_{\rm rel}$ is also a function of the hematocrit H. For simplicity, we assumed that $H = 0.45$, the average in humans.

2.2 Blood flow

To compute blood flow, vessels are treated as a network of pipes with radius r, volume flow rate q and wall shear force f. q is determined by Poiseuille's law *i.e.* $q \propto r^4/\eta(p_1 - p_2)$ given the hydrostatic pressure difference $p_1 - p_2$ at the attached nodes. The viscosity η is radius dependent, following [37], see fig. 1. For simplicity under the assumption of a homogeneous hematocrit of 0.45. As boundary condition the pressure is fixed at the arterial and venous roots of the vascular trees. Together with the mass conservation, *i.e.* inflow equal outflow rates at the nodes, we obtain a sparse linear equation system which is solved numerically.

2.3 Tumor cell density

Here we introduce a continuum model for the tumor cell density $c(\mathbf{r}, t)$. Under stress-free conditions without cell proliferation and death, the tumor cell density is $c^{(\rm norm)}$, which we assume to be $1/10\,\mu\mathrm{m}^3$, reflecting a typical lateral size of tumor cells of $10\,\mu$m. The dynamical evolution of the tumor cell density in the presence of cell proliferation and death is assumed to be given by a reaction-diffusion equation

$$\partial c/\partial t = -\nabla \cdot J + c^+ + c^-, \tag{1}$$

where J is the tumor cell flux and c^+ and c^- are source and sink terms describing cell proliferation and death, respectively.

In the following c^+, c^- and J are defined: We assume that tumor cells need sufficient oxygen to proliferate, which means that the local oxygen concentration o must exceed the threshold $o_{TC}^{(\rm prol)}$, else $c^+ = 0$. Moreover we assume that a maximum packing density $c^{(\rm max)}$ exists where cells are compressed so that they cannot proliferate further. We use the simplest expression to reflect that

$$c^+ = 1/t_{TC}^{(\rm prol)} c \left(1 - \frac{c}{c^{(\rm max)}}\right) \quad \text{if } o \geq o_{TC}^{(\rm prol)} \quad \text{else } 0, \tag{2}$$

where $t_{TC}^{(\rm prol)}$ is the mean proliferation time of unconstrained cells. Furthermore we assume that cells undergo apoptosis with the constant death rate $1/t_{TC}^{(\rm death)}$ if the local oxygen level o drops below $o_{TC}^{(\rm death)}$. The model includes this by the definition of c^-,

$$c^- = -1/t_{TC}^{(\rm death)} c \quad \text{if } o < o_{TC}^{(\rm death)} \quad \text{else } 0. \tag{3}$$

For simplicity, interaction with the resulting cellular debris is neglected. In the following the cell flux J is defined. We assume that cells migrate only in response to compression. Therefore a phenomenological "solid pressure" P is introduced. Its equation of state depends on the cell density c as follows: Below the density $c^{(\rm norm)}$ cells are not compressed, thus feel no forces, thus we set $P = 0$ for $c \leq c^{(\rm norm)}$. Else we define P as linear function which is zero for $c = c^{(\rm norm)}$ and increases to $P = 1$ for $c = c^{(\rm max)}$. In the style of Darcy's law, momentum terms in the equations of motion are neglected so that the cell migration speed is proportional to the driving force, which means that

$$J = -Dc\nabla P, \tag{4}$$

where D is an additional mobility constant. The cell density cannot exceed $c^{(\rm max)}$ since there are no external forces and $c^+ \to 0$ for $c \to c^{(\rm max)}$ even though P remains finite.

In the general framework of such a model it would be possible to add cell-cell adhesion. In this case one would consider volume fractions of other species, *e.g.*, normal tissue and necrotic tissue which interact via a free energy potential. See [21] and the references therein. The result is an effective surface tension force. Combined with expansive forces which drive the tumor rim outward, it can cause a fingering instability. In our simpler model where we have omitted such forces, tumor cells move diffusively opposed to their density gradient. Since tissue oxygenization is homogeneous on a coarse scale, this results in approximately spherically growing tumors. Biologically our model corresponds to a situation where tumor cells adhere to each other as much as to other cells. Also the tumor can expand without significant resistance from the surrounding tissue. We can justify this considering that i) not all tumors exhibit fingering instabilities, ii) we consider small tumor of less than 1 cm diameter and iii) pH level changes can happen that kill normal cells.

Below we compare our results with experimental data from melanoma. To accommodate the model to this specific tumor type, which can extend through multiple skin layers from the surface to muscle tissue, it would be straight forward to include inhomogeneous and/or anisotropic environments. We would expect this to trigger a different front shape of the growing tumor. However we think —as is the case with a "fingering" tumor— that the characteristics of the blood vessel network which we are interested would be invariant with respect to such additions.

In order to identify necrotic regions, we record the maximum local TC density over time. If the current TC density is zero and there were TCs in the past, we consider the location to be necrotic. On the basis of the rest of our framework, there are no forces that would impose interesting dynamics on the shape of necrotic regions. Thus we use this crude approximation.

The equations are discretized with a simple explicit finite-volume scheme on a cubic grid with $30\,\mu$m grid cell

size. We compute the fluxes through the cell faces separately. Knowing the fluxes, $\nabla \cdot J$ in (1) is discretized using a convective upwind scheme. To ensure stability, the time step for the integration is 0.1 h, whereas the updates of the rest of the system (see below) are done in 1 h steps.

2.4 Oxygen concentration field

The time scale for oxygen diffusion to reach a stationary state is of the order of seconds whereas the times scale for tumor cell proliferation, tip cell migration and endothelial cell proliferation is of the order of hours. Therefore we use for the oxygen concentration the quasi-static solution o of the diffusion equation, which adopts instantaneously any change in the source (vessels) and sink (tumor cells) configuration,

$$0 = \nabla^2 o - \gamma_o o + \alpha_o (o^{(B)} - o), \tag{5}$$

where γ_o is a consumption rate coefficient, $o^{(B)}$ the blood O_2 level and α_o a source coefficient. γ_o is a linear combination of the tissue specific constants $\gamma_o^{(\mathrm{norm})}$, $\gamma_o^{(\mathrm{tum})}$ and $\gamma_o^{(\mathrm{necro})} = 0$, for normal tissue, tumor tissue and necrotic regions, respectively. The definition of the density parameters implies that the necrotic areas inside the tumor do not consume oxygen. The factor α_o determines the amount of extravasated oxygen per concentration difference at the vessel wall. It is defined as permeability times wall surface area per concentration and tissue volume. For simplicity it assumes a constant value for all blood circulated vessels. $o^{(B)}$ is the oxygen concentration in blood plasma, for which local variations are also neglected.

The coefficients γ_o and α_o comprise the diffusion constant and therefore it does not appear in (5). We estimate γ_o based on the diffusion range R_o of oxygen around isolated vessels found in tumors. Therefore we use that a delta peak as source distribution generates an exponentially decaying radial profile $\exp(-x\sqrt{\gamma_o})$. Thus R_g is of the order of $1/\sqrt{\gamma_o}$. The parameter $o^{(B)}$ is determined such that, given γ_o, the concentration between vessels is ca. 50% of the concentration at the vessel wall.

2.5 Growth factor concentration field

The growth factor concentration g is computed by a Greens' function-like method. Underoxygenized tumor cells, which means that locally $o < o_{TC}^{(\mathrm{prol})}$, produce growth factor at a constant rate. It diffuses through the tissues and degrades with a constant rate. Therefore each source cell produces an exponentially decaying distribution. Thus we can write g as

$$g(\boldsymbol{x}) = \int \mathrm{d}^3\boldsymbol{x}'\, G(\|\boldsymbol{x}' - \boldsymbol{x}\|)\, \theta(o_{TC}^{(\mathrm{prol})} - o(\boldsymbol{x}'))\, c(\boldsymbol{x}'), \tag{6}$$

where θ is the Heaviside step function. For simplicity we define $G(x) \propto \max(0, 1 - x/R_g)$ as a linearly decaying normalized function which vanishes at $x = R_g$, where R_g is a "diffusion range" and limits the region where angiogenesis is induced.

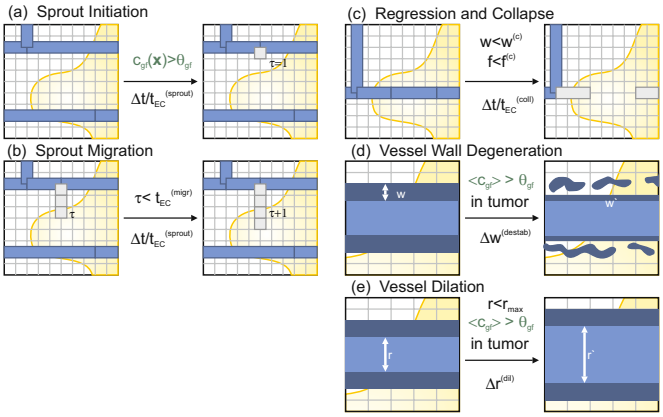

Fig. 2. (Colour on-line) Sketch of the vessel network remodeling processes. Initial/final states are shown to the left/right of the arrow with the rate parameter below and essential preconditions above the arrow. Vessel segments are shown as blue bars, the tumor is depicted as yellow mass and the underlying lattice is illustrated in the background. (a) A new sprout is generated by potentially splitting an existing segment, adding a node and adding the new sprout segment. (b) A sprout is extended by adding further segments to its tip. (c) Vessel regression is modeled by removal of respective segments. This can disrupt blood flow, leaving non-circulated vessels which are depicted in gray. (d) Vessel walls degenerate within the tumor due to detachment of support cells. This is modeled by a decreasing maturation parameter and depicted here as decreasing wall strength and surrounding debris. (e) Within the tumor vessels dilate. See text for details.

2.6 Vessel network remodeling dynamics

The evolution of the network is subject to three stochastical processes: sprout initiation, sprout migration and collapse as well as continuous wall degeneration and vessel dilation (fig. 2). The definition of these processes closely follows the definition in [29], where 2d networks are considered. Therefore we only give a brief description here and refer in particular for the biological motivation of the details to [29].

Sprout initiation: A new vessel segment can be added with probability $\Delta t / t_{EC}^{(\mathrm{sprout})}$ at any location on the network if the local growth factor concentration is non-zero, the distance to the next branching point is less than $l^{(\mathrm{spr})}$ and the time spent within the tumor is less than $t_{EC}^{(\mathrm{switch})}$. "Within the tumor" is defined as $\langle c \rangle > c^{(\mathrm{norm})}/2$ averaged over the segment. The new segment occupies an edge on the lattice (length Δl) and points in the direction of the largest growth factor increase.

Sprout migration: Those segments are tagged as sprouts, which means that further segments can be attached with probability $\Delta t / t_{EC}^{(\mathrm{sprout})}$, extending the original sprout. Sprouts can also spawn sub-sprouts like normal vessels can. They are, however, excluded from the collapse, degeneration and circumferential

growth mechanisms. Sprout vessels are untagged and become normal vessels if the tip fuses with another vessel such that blood can flow, or if their respective lifetime variable τ, which every sprout has attached, has reached its predefined maximum $t_{EC}^{(\mathrm{migr})}$. If the tip fuses with another sprout without creating a conducting branch, it remains tagged as sprout.

Wall degeneration: The structural support provided by the cell layers surrounding the endothelial cells is represented by the wall stability variable w. For new vessels and the original vasculature it is initialized with the wall thickness of healthy vessels, see [29]. For vessels inside the tumor its value decreases at the constant rate Δw until zero.

Vessel collapse: A segment can be removed with probability $\Delta t/t_{EC}^{(\mathrm{coll})}$ if its wall stability variable w is zero and the wall shear stress f is below the threshold $f^{(\mathrm{coll})}$.

Vessel dilation: The vessel radius r increases at the constant rate k_r if $r < r^{(\mathrm{max})}$, the average growth factor concentration over the segment is non-zero and if the time spent within the tumor is larger than $t_{EC}^{(\mathrm{switch})}$.

Per time step ($\Delta t = 1\,\mathrm{h}$), a Monte Carlo sweep is done per stochastical process and all continuous variables and fields are advanced in time. The parameter values that we use throughout the paper are given in table 1 (references to physiological data are given in [25,27,29]).

The model is stable with respect to parameters, since our observables vary smoothly with parameter deviations. For brevity we omit an analysis here. In our previous papers [25,27] we have discussed variations for 2d models which are also relevant for the present study.

Table 1. List of parameter values used for all simulations.

Parameter	Value	Description
N	800	Lattice size
Δl	$10\,\mu\mathrm{m}$	Lattice constant
Δl_V	$60\,\mu\mathrm{m}$	Lattice constant (tree construction)
D	$300\,\mu\mathrm{m}^2/\mathrm{s}$	TC mobility
$c^{(\mathrm{norm})}$	$1/(10\,\mu\mathrm{m})^3$	Normal cell density
$c^{(\mathrm{max})}$	$2/(10\,\mu\mathrm{m})^3$	Maximum cell density
$o^{(B)}$	1	Blood oxygen level
α_o	$0.004/\mu\mathrm{m}^2$	O_2 source coefficient
$\gamma_o^{(\mathrm{norm})}$	$1/(100\,\mu\mathrm{m})^2$	O_2 consumption coefficient by normal cells
$\gamma_o^{(\mathrm{tum})}$	$2/(100\,\mu\mathrm{m})^2$	O_2 consumption coefficient by tumor cells
R_g	$200\,\mu\mathrm{m}$	Growth factor diffusion range
$t_{EC}^{(\mathrm{switch})}$	24 h	Sprouting/Dilation switch delay
$t_{EC}^{(\mathrm{sprout})}$	$5\,\mathrm{h}/10\,\mu\mathrm{m}$	Sprout extension time
$t_{EC}^{(\mathrm{migr})}$	100 h	Sprout activity duration
$l^{(\mathrm{spr})}$	$20\,\mu\mathrm{m}$	Sprout sites minimum separation
$r^{(\mathrm{sprout})}$	$4\,\mu\mathrm{m}$	Initial sprout vessel radius
k_r	$0.4\,\mu\mathrm{m/h}$	Vessel dilation rate
$r^{(\mathrm{max})}$	$25\,\mu\mathrm{m}$	Maximum dilation radius
$t_{TC}^{(\mathrm{prol})}$	10 h	TC proliferation time
$t_{TC}^{(\mathrm{uo})}$	100 h	Hypoxic TC survival time
$f^{(\mathrm{coll})}$	2 Pa	Critical wall shear stress
$t_{EC}^{(\mathrm{coll})}$	20 h	Unstable vessel survival time
Δw	$0.05\,\mu\mathrm{m/h}$	Dematuration (w) rate
$o_{TC}^{(\mathrm{death})}$	0.01	TC hypoxia O_2 threshold
$o_{TC}^{(\mathrm{prol})}$	0.1	TC proliferation O_2 threshold

2.7 Arterio-veneous tree construction

The vasculature in real tissue exhibits a tree-like structure. Few thick arteries branch out into arteriolar microvessels. Terminal branches are connected to the capillary bed, a dense network consisting of thin vessels where most of the exchange with the surrounding tissue happens. Further upstream blood is collected in venules which fuse into thick veins. The design goal of such a structure is to provide a sufficient supply of nutrients to all regions of the tissue, while minimizing the energy necessary to maintain the circulation.

In [35] a method was presented to construct representations of vascular trees stochastically according to probabilistic rules that depend on local system properties. The construction of the blood vessel network is based on the stochastic remodeling of a collection of binary trees. Each tree represents either an arterial or a venous branch. Analogous to the definition of the tumor growth model, the tree edges coincide with the edges of a cubic lattice, and have associated hydrodynamic properties. The remodeling is executed in successive sweeps where tree leaves are removed or extended depending on the wall shear stress in the parent edge. Thereby moves that would result in overlapping nodes are rejected. The initial configuration is generated by first placing tree roots randomly at the boundary sites of the lattice, followed by random growth until the lattice is filled. Blood flow is computed between remodeling sweeps. Prior to that, the individual trees are connected by "capillary" edges, which are temporarily added between leaves of opposing type. For brevity we refer the reader to the appendix of [29], where the procedure is described in detail for a triangular 2d lattice. The difference to the cubic 3d case considered here lies in the number and location of root nodes and the pieces appended at nodes where growth happens. Here we chose initial locations of the root nodes randomly according to a uniform distribution over the system domain faces. Arterial and venous types are selected in alternating order. A new location is rejected if it is closer than $N\Delta l/10$ to either another root or an edge of the system domain. The

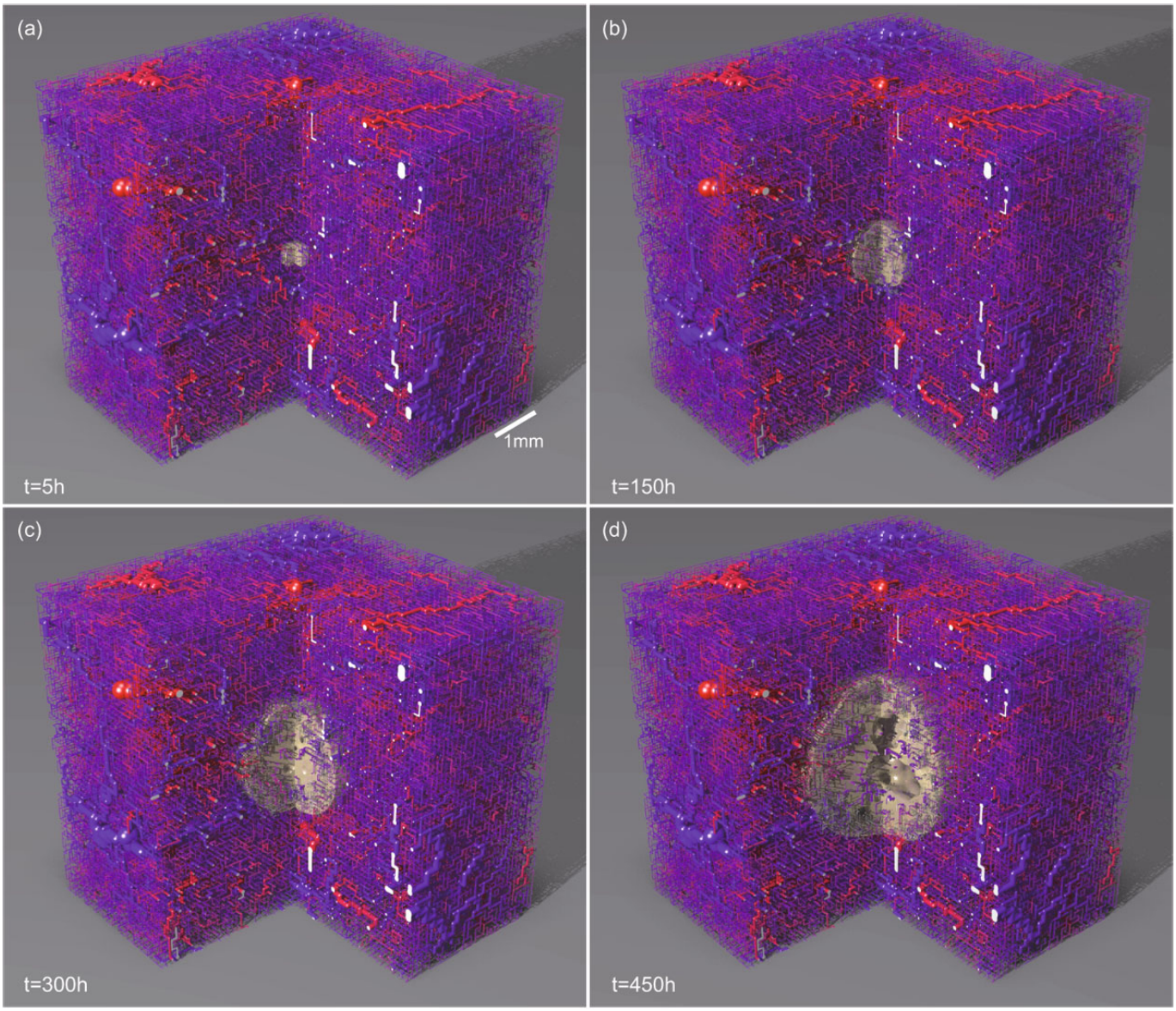

Fig. 3. Visualization of the vessel and tumor configuration generated by a simulation of the model at different times. A cut through the cubic simulation volume is shown. The vessels are depicted as cylinders which are color coded by their blood pressure (blue = 0 kPa; red = 12 kPa). Non-circulated vessels are shown in gray. The spheroid in the center shows the isosurface where the tumor cell density equals 50% of the normal packing density $c^{(\mathrm{norm})}$.

growth pieces are selected from three planar configurations: a single edge, a $\dashv$ shape consisting of three edges, and a $-\sqsubset$ shape consisting of five edges. The latter two should approximate the more realistic Y shapes in real vasculatures. Among all admissible configurations and orientations, one is randomly picked.

While it is highly non-trivial to synthesize vascular networks that are realistic in every way possible, our initial networks exhibit reasonable hierarchical structures, spatial distributions of the capillaries, and agreement with the flow data in [35] and the experimental references therein. Figure 6 shows analogous plots which can be used for comparison. They are discussed with respect to the tumor network in sect. 3.2.

3 Results

In fig. 3 we show snapshots of the dynamical evolution of the tumor and vessel network configuration at successive times. Initially the tumor O_2 consumption leads to decreased O_2 levels within the nucleus and consequently enables vascular remodeling via growth factor production of the TCs. The sprouting process first creates a dense capillary plexus which provides more oxygen and facilitates tumor growth. Vessel collapses begin after a few days ($t = 200$ h). Small capillaries collapse immediately under bad perfusion while thicker vessels survive longer due to their stability, *i.e.* large w, independent of blood flow until they become unstable. The network is thus progressively

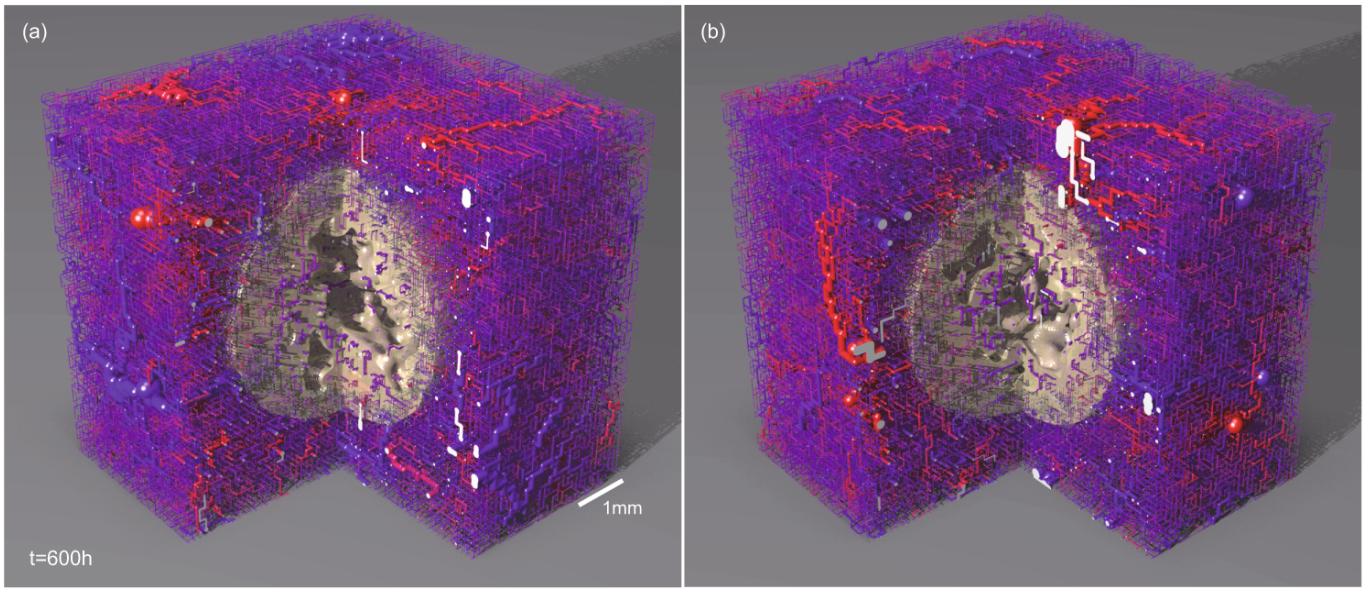

Fig. 4. Left: final configuration (at time $t = 600\,\mathrm{h}$) of the simulation run shown in fig. 3. Right: for comparison a final configuration resulting from a simulation run that started with a different initial arterio-venous network. Generally one observes that the MVD behind the tumor rim is increased due to a large number of sprouting vessels. Most of them are not viable because they cannot form blood circulated circuits, in addition also many original capillaries regress. The tumor becomes interspersed with a few isolated, dilated vessels. The lack of oxygen in non-perfused regions leads to the empty (necrotic) regions in the center.

remodeled, predominantly within a thin band around the tumor boundary. The sparse network left in the center remains static except for few collapses of isolated threads.

The resulting network morphologies shown in fig. 4 display the typical high-MVD periphery and low-density center. The remaining internal vessels form short-cuts between arteries and veins which touch the tumor surface. This is a consequence of the dilation that all vessels undergo in the tumor. The short-cuts consist of neovasculature as well as parts of the initial vasculature.

Starting with different initial arterio-venous networks yields different final configurations, as shown in fig. 4, but their global characteristics, as quantified by the radial distribution functions analyzed in the next subsections, do not vary significantly.

The tumor masses grow approximately sphericaly. After a short initial phase their radius increases linearly, since proliferation is predominantly restricted to the boundary where sufficient space and oxygen is available. The cell density profiles c exhibit steep slopes at the invasive edges, dropping from $c^{(\mathrm{norm})}$ to zero. In the tumor interior c fluctuates between zero and $c^{(\mathrm{max})}$, depending on oxygenization.

3.1 Radial distributions

Figure 5 shows the tumor density (in all panels), average vessel radius (panel a), microvascular density (MVD, panel b), oxygen concentration (panel c), blood flow rate through the vessels (panel d), vessel wall shear force (panel e) and growth factor concentration (panel f) as a function of the radial distance r from the tumor center for different times. The data are averaged over 50 simulation runs with different initial networks and over concentric spherical shells centered around the tumor center. The microvascular density (MVD) is defined as the volume fraction occupied by the vessels. The quantities which are associated with vessel segments (radius, flow, shear force) are averaged over the number of vessel-occupied lattice sites within the respective shells.

In each panel the radial tumor density at the appropriate times is represented by broken lines: it facilitates the comparison of various features of the vessel quantities with the tumor extension. The peak in the radial tumor density indicates the boundary of the tumor (stochastic fluctuations within the shells as well as from sample to sample cause the finite width of this step). Since the individual curves are for equidistant times, it is clear from the linear shift of the peak density that the tumor radius grows linearly in time. Behind the peak, at smaller distances r from the center, the tumor density drops monotonously, reflecting the emergence of necrotic zones in the tumor center.

The MVD in panel (b) of fig. 5 has a peak in the peritumoral region, *i.e.* outside of the tumor at a distance slightly larger than the peak of the tumor density. It is 1.5 to 2 times higher than the normal MVD (plateau value at large distances). Inside the tumor (at small distances) the MVD drops monotonously to zero (at long enough times), again reflecting the emergence of the necrotic core.

Correlated with the peak in the MVD is a small peak in the oxygen concentration (panel (c) of fig. 5), and a dip in the average vessel radius (panel (a)), the average flow

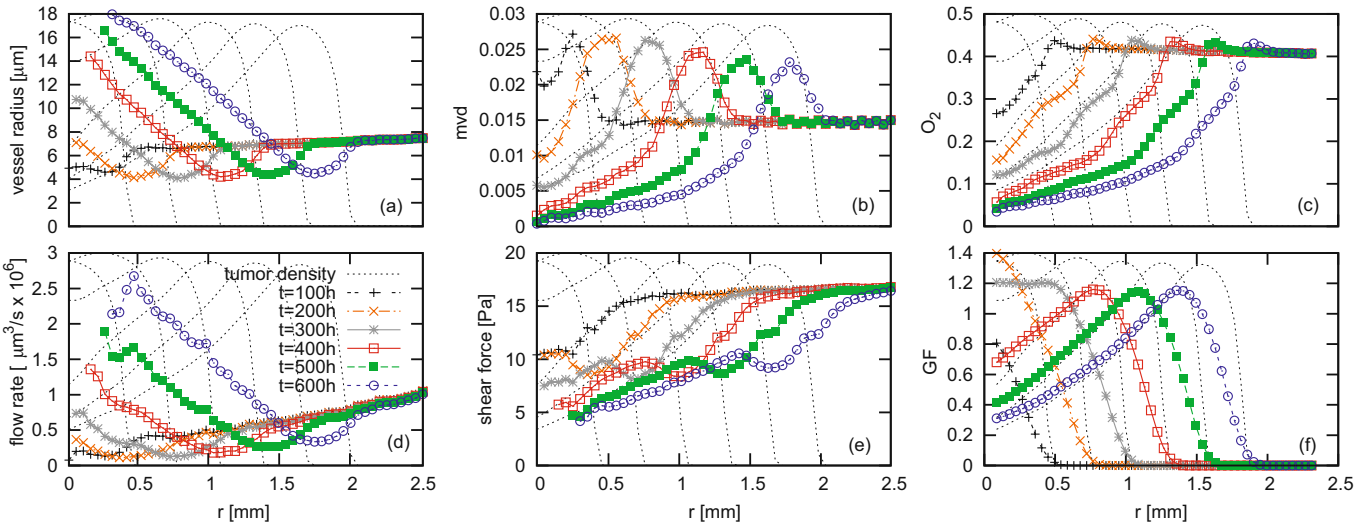

Fig. 5. Results for (a) vessel radius, (b) microvascular density (MVD), (c) oxygen concentration, (d) blood flow rate through the vessels, (e) vessel wall shear force, and (f) growth factor concentration as a function of the radial distance from the tumor center for different times (see lower left panel for legend). The broken lines indicate the radial tumor density at the times corresponding to the other data shown.

rate (panel (d)), and the average shear force (panel (e)): The peak in the MVD in the peritumoral region reflects the presence of many new capillaries, which increase the oxygen supply but simultaneously decrease the average vessel radius since capillaries have minimum radius. Furthermore, since the average blood flow that is supplied by the arterio-venous network is approximately constant, this flow has to be distributed over 50–100% more microvessels in the tumor perimeter, which induces a reduction in average flow rate and shear force.

Within the tumor (*i.e.* for distances smaller than the location of the peak of the MVD) the vessel radius increases monotonously with decreasing distance from the tumor center (panel (a) of fig. 5), which is the effect of the switch from angiogenic sprouting to circumferential growth within the tumor. The axial blood pressure gradient within the vessels, $\mathrm{d}p/\mathrm{d}l$, which is not shown here, decreases monotonically with decreasing distance from the tumor center by more than one order of magnitude. Although the pressure gradient decreases, the average blood flow rate (q, panel d) within the vessels increases towards the tumor center, since it is proportional to the 4th power of the vessel radius R, $q \propto R^4 \mathrm{d}p/\mathrm{d}l$. The average shear force f is proportional to the 1st power of R, $f \propto R\,\mathrm{d}p/\mathrm{d}l$, therefore it decreases with decreasing distance from the center.

The average oxygen concentration (panel c) decreases rapidly towards the tumor center and drops below the GF production threshold $o_{TC}^{(\mathrm{prol})} = 0.1$ (relative to normal oxygen) at approximately the same distance $r_{\mathrm{low\,oxy}}$, where the growth factor concentration (GF, panel f) displays a peak. This peak is therefore not at the same position as the peak of the tumor density. For distances smaller than the "underoxygenization radius" $r < r_{\mathrm{low\,oxy}}$, all tumor cells produce GF and the shape of the GF concentration *versus* distance r is identical with the tumor density.

MVD and vessel radius show the typical compartmentalization that has been observed in melanoma [4,5] and glioma [36]: For instance in [4] the MVD and vessel radius were measured in three distinct regions of human and mouse melanoma: the central region, a 100 μm wide peripheral band just behind the invasive edge, a 200 μm wide peritumoral region outside the invasive edge. In the central region, they found a MVD that was reduced to 25% of the MVD of normal tissue, and increaesd up to 200% in the peritumoral region. They found that the vessel perimeter grew linearly from 50 μm to a plateau at 200 μm by day 15.

In contrast to our results for regular vascular networks [25–27], flow rates and shear force now show a plateau similar to the vessel radius. In [25–27] the fixed pressure gradient along the boundaries of the regular (rectangular or hexagonal) networks led to unrealistic star-shaped morphologies, directing all blood flow through the center. The hierarchical initial networks that we consider here do not have these artifacts and display a physiologically realistic morphology.

3.2 Vessel statistics

Figure 6 shows scatter plots of hemodynamic variables against the vessel radius r, which are in good agreement with those obtained in [35]. The plots combine samples throughout the full vasculature from all runs at $t = 400$ h.

We generally observe that the variance of the flow-related parameters increases drastically towards the capillaries. This might be an artifact of our initial network construction, but averaged quantities display physiologically sound characteristics.

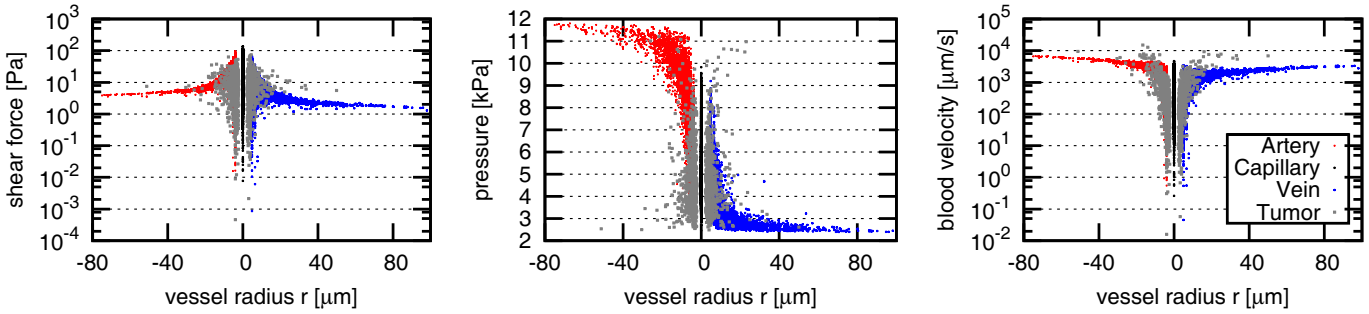

Fig. 6. (Colour on-line) Scatter plots of vessel-related hydrodynamic quantities —shear force, pressure, and blood velocity— against the vessel radius r (each dot corresponding to one vessel). Red dots (to the left with negative radius for better visibility) correspond to arteriolar vessels, blue dots (to the right) to venous vessels, black dots (at $r = 0$) to capillaries, gray dots to tumor vessels. The latter are randomly plotted on either side (arteriole or venous) because they do not exhibit a clear hierarchical distinction. The plot combines samples uniformly distributed over the full vasculatures of all simulation runs at $t = 400\,\mathrm{h}$.

The blood pressure plot shows that the tumor vessels tend to exhibit low blood pressure. The few larger tumor vessels ($r > 10\,\mu$m), however, show a more uniform distribution. The velocity plot shows that these vessels have high blood flow rates, whereas the average for capillaries is about one order of magnitude lower. Both observations support the view that tumor-internal vessels form short-circuits between arteries and veins intruding into the tumor rim. Responsible for this is the vasodilation mechanism which acts on all tumor vessels and decreases their flow resistance.

Compared to hierarchical 2d networks [29], flow parameters are distributed similarly. However, a few details are apparent. i) The sigmoidal shape of the pressure distribution seems to be more pronounced. ii) The shear force in the arteries decreases for large r whereas it increases for the 2d networks. iii) In fig. 7 of ref. [29] one could observe tumor vessels which have reached the maximum dilation radius and exhibit flow parameters spanning over several orders of magnitude. We think that i) and ii) can be attributed to the three dimensionality of the system which enables different initial network geometries to emerge. iii) is the result of the shorter simulation time, since most tumor vessels might not reach the maximum dilation radius.

3.3 Fractal dimension

The vascular tumor network is extremely inhomogeneous and has geometric, in particular fractal, properties that are very different from normal vasculature [38]. The concept of a fractal dimension is often used to characterize differences between normal vasculature and tumor vasculature [38,39].

One commonly used method to estimate fractal dimension is box-counting, which is carried out by superimposing boxes of size ϵ arranged as a regular grid on the fractal object and counting the number of boxes N_ϵ which overlap the object. The self-similar nature of true fractal object leads to the power law $N_\epsilon \propto \epsilon^{-D_f}$, where N_ϵ is the number of overlapping boxes. D_f is usually extracted by a linear fit in a log-log plot. However in experiments one can usually measure ϵ at most over two orders of magnitude. Furthermore natural objects (or rather photographs thereof) are usually not perfectly fractal *i.e.* box-counting plots exhibit non-constant slopes. Therefore even a small constant regime is often considered sufficient to speak of a fractal dimension (or more truthfully named box-counting dimension); see the discussion in [41]. Therefore what we mean in the following with "fractal dimension" is the number that we obtained by the procedure described below and which is analogous to the way in which this number is extracted from the analysis of experimental data [38,39,41].

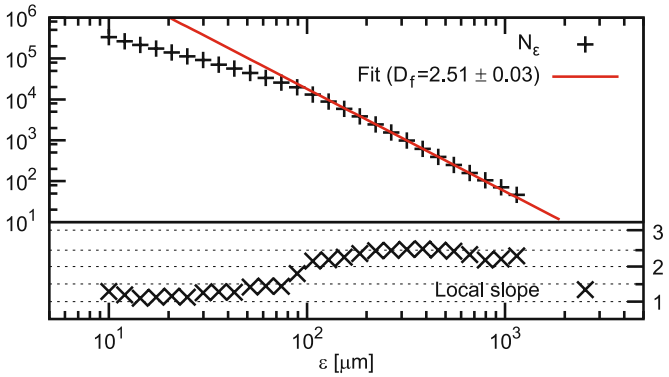

Fig. 7. Top: log-log plot of the box counts N_ϵ against the box size ϵ for the determination of the fractal dimension of the tumor vasculature of one final system. For the intersection with the boxes, the vessels were approximated as lines. An estimate for the fractal dimension is obtained from the best fit to $N_\epsilon \propto \epsilon^{-D_f}$. Bottom: the data represent the (negative) local slopes of the data points for N_ϵ in the log-log plot above.

For the application of the box-counting procedure, our vessel networks are approximated as a collection of line segments. For the measurement of the tumor network we discard segments which are not within the tumor ("within the tumor" is where $\langle c \rangle > c^{(\mathrm{norm})}/2$, see sect. 2.6). Our data for $\log(N_\epsilon)$ as a function of $\log(\epsilon)$ do not follow a straight line as one would expect if $N_\epsilon \propto \epsilon^{-D_f}$ but are slightly bended, see upper panel of fig. 7. From the data we can extract the local slopes and plot them as a function of ϵ as done in the bottom panel of fig. 7. At small box

sizes the local slopes are close to -1, reflecting the fact that in the analysis we assumed the vessel segments to be 1-dimensional objects. For larger box sizes the local slopes start to reflect the network geometry (rather than the geometry of individual vessels) and we can consistently identify a small plateau at $D_f \approx 2.5$, which we take as our estimate for the fractal dimension of the vessel network: $D_f = 2.5 \pm 0.03$ on average. This is in very good agreement with the value obtained earlier for regular cubic initial networks (in 3d) $D_f = 2.52 \pm 0.05$ [26].

In [26] it was hypothesized that the fractal properties of the emerging tumor vasculature are independent of the initial (3d) blood vessel network. Our present finding that D_f of the tumor vasculature for a 3d arterio-venous initial network is close to D_f for 3d regular initial networks supports this hypothesis.

We also checked the non-capillary parts of the initial network and obtained with equally well matching fits $\langle D_f \rangle = 1.46$ for arteries, $\langle D_f \rangle = 1.51$ for veins, and $\langle D_f \rangle = 1.64$ for both combined, which is close to the estimate for real arterio-venous subcutaneous vascular networks [39].

Moreover, in [25,26] we identified the basic mechanism responsible for the fractal properties of the tumor vasculature as the stochastic, blood flow correlated removal of vessels via vessel collapse and regression, denoted as flow correlated percolation (see also [42]).

3.4 Spatial inhomogeneities and hot spots

"Hot spots" are regions of increased blood flow within the tumor. It is possible to compare our results at least qualitatively with clinical imaging of tumor blood flow using tomography techniques, *e.g.* [43]. Therefore we generated maps of local average flow velocities $\langle v \rangle = \frac{1}{|C|} \int_C v(\boldsymbol{x}) \mathrm{d}\boldsymbol{x}$, where C is a small subvolume, $v(\boldsymbol{x}) = q/\pi r^2$ is the flow velocity at locations within a vessel and zero everywhere else, and q denotes the flow rates of the respective vessels. The integral is evaluated stochastically. An example is shown in fig. 8. Analogous to imaging experiments, we can find regions of zero flow and so-called hot spots with high velocities. Unperfused regions coincide with necrotic regions by design of our model. Likewise, hot spots are identified by vessels threading the tumor. Since the tumor vessels have high flow rates and are dilated, even one such vessel can show up as a "hot spot". Our model thus supports the hypothesis raised in [43] that hot spots are due to highly conductive arterio-venous shortcuts.

In 2d [29], one could observe the formation of dense vessel clusters accompanying the predominant isolated strings of surviving vessels in the tumor center. It could be shown that these clusters are more likely to form in regions with high hydrodynamic pressure differences between neighboring vessels. A map of these pressure differences can be constructed by determining the solution of the Laplace equation for a pressure field $p(\mathbf{r})$ defined on the space between the vessels with the boundary condition that $p(\mathbf{r})$ is identical to the blood pressure inside the vessel at location $\mathbf{r}$. Thus, the field $p(\mathbf{r})$ interpolates the pressure between vessels. The (local) gradient magnitude $|\nabla p|$ of this map for the original vasculature shows positive correlation with the (local) microvascular density in the emerging tumor vasculature in 2d [29].

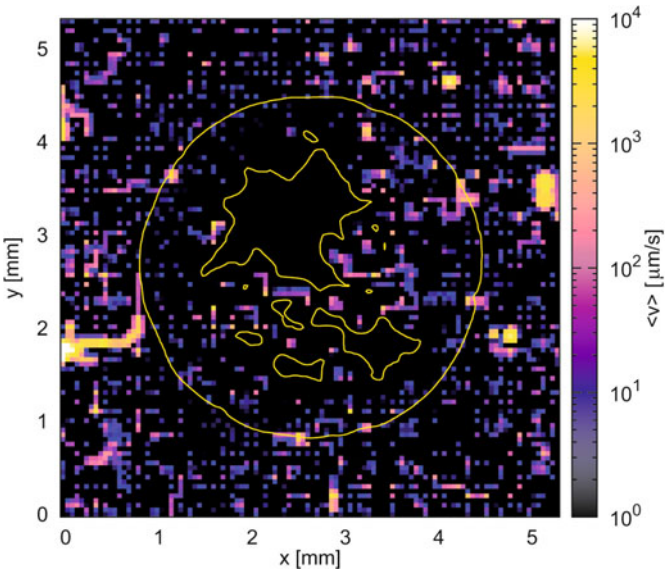

Fig. 8. (Colour on-line) Local flow velocity distribution in a slice through a tumor vasculature. The yellow line shows the $c^{(\mathrm{norm})}/2$ isocontour of the tumor cell density. The plotted quantity is the blood flow velocity averaged over $(50\,\mu\mathrm{m})^3$ grid cells. The resulting image is reminiscent of MRI blood flow studies and shows regions with low flow and hot spots. Since we did not incorporate the interstitial flow, the distribution is zero where vessels are absent.

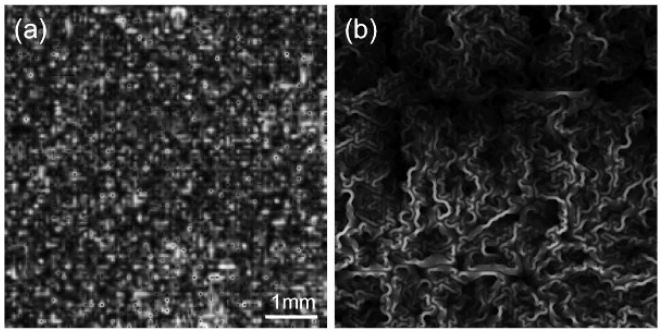

Fig. 9. Local values of $|\nabla p|$ are shown, where $p(\mathbf{r})$ is a continuous field which interpolates the blood pressure between neighboring vessels of an initial network configuration. (a) Shows a slice through the center of a 3d system considered here and (b) shows the result for a 2d network obtained in [29]. While in (b) large-scale fluctuations can lead to dense clusters of internal tumor vessels, (a) is comparably homogeneous and the tumor networks consist of isolated strings in the tumor interior.

However, dense vessel clusters observed in 2d [29] are absent in the tumor vasculature emerging from the 3d arterio-venous networks considered here. Concomitantly the pressure (gradient) fields for the 3d initial networks considered here are more homogeneous, except on a very short scale between neighboring vessels. Figure 9 demonstrates this by a comparison of the pressure gradient $|\nabla p|$

for (a) a 3d initial network and (b) a 2d network. The spatial variation of the pressure gradient $|\nabla p|$ is determined by the geometry of the initial vessel network, which again depends on the precise location of the roots of the arterial and venous trees (sources and sinks) and the details of the construction algorithm. We think it would be possible to construct an arterio-venous initial network in 3d, where results would resemble those reported for 2d in [29], see fig. 9(b), but we have not checked this yet.

4 Drug transport

To analyze the effectiveness of blood-borne drug transport to a tumor and its distribution inside, a time-dependent concentration profile over the vasculature is propagated according to the local blood flow velocities. A corresponding mathematical model was presented [17] for a pure vessel-in-growth capillary network, originating from a single parent vessel. We adopted this method to check whether there are similar obstacles to successful drug delivery inherent to the tumor vascular networks.

The starting point is a given configuration for the vasculature with precomputed variables for flow, flow velocity, vessel length, and radius. In addition, a mass parameter m is associated with each vessel describing the amount of drug in the blood volume contained in the vessel. The mass content m is deterministically updated in successive time steps as follows: First the drug amount flowing out of vessels is determined and added to corresponding node mass variables. Under the assumption of perfect mixing, the nodal masses are then redistributed into further downstream vessel. Thereby mass conservation is strictly enforced. A detailed description can be found in [27,17]. The most severe limitation of this model is that there is no exchange with extravascular space and therefore also no uptake by the tumor.

The results in the following were obtained with continuous injections into the final tumor networks. Initially the networks are filled with "clean" blood. Extravasation of drug is neglected.

When drug is inserted simultaneously through all arterial inlets, it is distributed very rapidly over the whole network. Within the order of several seconds the network is saturated with the maximum drug concentration. To illustrate that, fig. 10 shows a sequence of snapshots over 5 seconds. At the tumor border, where the MVD is high and the network contains many loops, there may be tiny regions (ca. 100 μm diameter) that take an order of magnitude longer to fill. Note also that the dilated tumor vessels through the center conduct very well and act as short-circuits between arteries and veins. The outer regions of the system where the network remains normal can also transport drug towards the tumor periphery. Therefore the tumor as a whole is well perfused.

In [17,18] it was predicted that large amounts of drug bypass the tumor, varying by an order of magnitude depending on parameters. Drug bypassing also occurs naturally in our model since all vessels (original and tumor) are perfused with drug after ca. 5 s (see fig. 10). This is independent of the details of the vasculature be it from healthy or pathological tissue: whenever one wants to hit a specific region of the vascularized tissue with a blood-borne drug, one has to inject it into a high-level artery which also branches into parts outside the target region. The more relevant question therefore is: How long, during an injection of length δt, are all target vessels exposed to a drug concentration larger than a predefined threshold? For realistic situations the question "how much drug volume" bypasses the tumor is somewhat ill-defined, since the answer depends on the level of the arterial tree one injects the drug in.

We analyzed how long tumor vessels are exposed to a drug concentration larger than a predefined minimum drug level c_{thres} and show the result in fig. 11. It confirms the former visual impression that drug perfusion is fast: For instance, in our 30 s simulation time over 90% of the vessel network was exposed to at least $c = 0.5$ for at least 25 s, and 99% for at least 15 s. Also the curves for $c_{\mathrm{thres}} = 0.5$ and 0.01 nearly match, from which one can conclude that drug advances through the network with a sharp front, exposing vessels "on contact" instantly to high drug concentrations.

Although we consider here continuous drug infusions, a bolus injection of fixed drug volume or limited time should be extremely short (less than 5 seconds) in order to be distinguishable from a continuous infusion due to the speed at which drug is transported. Therefore our predictions are also relevant for bolus injections longer than 5 seconds.

Qualitatively the results for drug flow reported here agree with those for 2d arterio-venous networks [29]. A notable difference is that in 2d the tumor networks can disrupt the flow in larger regions ($\gg 100\,\mu$m diameter) than here, which also extend into sections of the original network. This is because the initial network configurations considered in [29] have fewer pathways to major feeding vessels. Therefore blood flow to aforementioned regions passes through the comparably badly conducting tumor boundary, resulting in low flow rates.

We remain with our conclusion that experimentally observed deficiencies in drug delivery must have other reasons, and these most probably lie within the characteristics of extravasation of drug and interstitial fluid transport within the tumor, which we did not include into the present version of our model.

5 Discussion

In this paper we formulated a hybrid cellular automaton model to analyze the vascular remodeling process of three-dimensional arterio-venous vessel networks during solid tumor growth. The model involves sprouting angiogenesis, vessel co-option, dilation and regression as well as tumor cell proliferation and death. It predicts that the tumor vasculature emerging from the interplay of these processes is non-hierarchical and compartmentalized into a highly vascularized tumor perimeter, a tumor periphery with large vessel density and dilated vessels and a central region containing necrotic regions with a low microvascular density

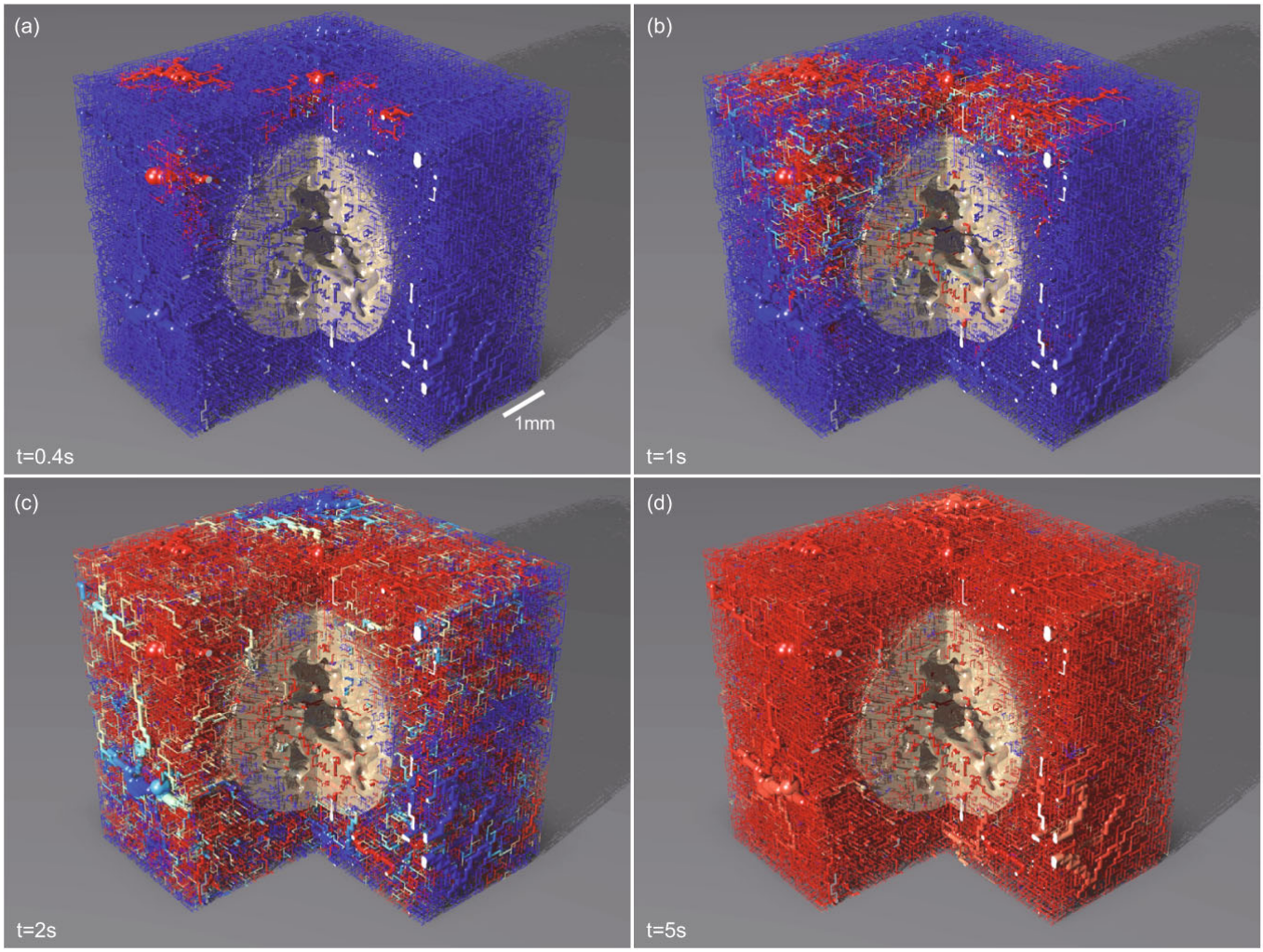

Fig. 10. (Colour on-line) Snapshots of a drug flow simulation in a tumor vessel network produced by our model. The color code shows the dimensionless concentration (red: 1; blue: 0). The drug is injected with the initial concentration 1 at the arterial root nodes. The transport is very effective. Already after 5 s the vasculature is almost completely saturated.

threaded by extremely dilated vessels. This is a general feature of the remodeling process of the normal vasculature into the tumor vasculature in the model, and we propose this to hold also for *in vivo* tumor: none of the initial characteristics of the original vessel network survives this process. In this work this proposition was demonstrated for a 3d arterio-venous initial network, and analogous observations have been made for 2d arterio-venous initial networks [29] and for regular networks consisting of capillaries of equal diameter arranged in a regular grid with a given MVD, in 2d [25] and 3d [26]. Once the tumor grows over it, it gets transformed into a compartmentalized network with irregularly arranged dilated vessels and a decreasing MVD from the tumor periphery to the tumor center, resulting in an inhomogeneous oxygen distribution.

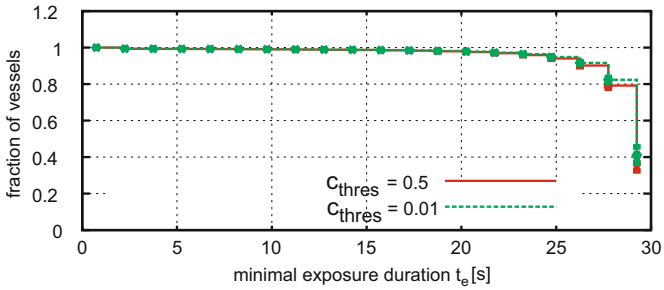

Fig. 11. Exposure durations: A point in the diagram means that a certain fraction of the vessel network is exposed to a drug concentration larger than c_{thresh} for a duration longer than t_e. Simulation time: 30 s.

5.1 Comparison with earlier work in 2d and 3d

Before more general conclusions are discussed, we highlight some notable differences and similarities of the results of our model systems. The global morphology of the vascular tumor networks, as reflected by measurements of radial distributions of various parameters agrees qualitatively very well in all of our model versions. Quantitative differences arise primarily in the flow rate distributions

since these depend strongly on the network morphology. Moreover, the vessel statistics of arterio-venous initial networks agrees very well in 2d [29] and 3d (fig. 6), and also with [35] from where we adopted the initial network construction method.

Concerning the emerging tumor vessel network morphology, significant differences to the results reported here exist for regular initial networks [25–27]. In these studies a linear blood pressure gradient was imposed as a boundary condition which drives blood from from one corner of the simulation domain to the opposite corner. This aligns surviving tumor vessels in the flow direction, and can even impose artifacts where vessels converge to a singular point in the center of the tumor. These artifacts are absent in hierarchical arterio-venous initial networks studied in this paper and in [29]. Resulting tumor networks are isotropic, but may not be homogeneous. One can divide them into sections which consist of dense clusters of capillaries and on the other hand vessels which thread the tumor as isolated strings. We can attribute their relative occurrence to the morphological details of the initial networks —location of major feeding/draining vessels in particular.

Analysis of the fractal dimension D_f (see below) can give valuable insight into the fundamental mechanism of the emergence of the specific tumor network morphology. In all of our model systems the value for D_f agrees reasonably well with the value of the fractal dimension of the critical percolation cluster in site percolation, either in 2d [25, 29] or in 3d, [26] and this study.

Lastly, our simulations show that drug transport is much more efficient for arterio-venous networks than for regular (capillary) networks [27]. The latter case is not a very realistic choice for transport studies, since it lacks the fast pathways provided by arteries and veins. For grid-like initial capillary networks it takes ca. 60 seconds for drug to travel from one end of the system to the other. Arterio-venous networks, in contrast, both in 2d and 3d, lead to the saturation of 90% network with drug, including the tumor section, within ca. 6 s. There are isolated regions where vascular remodeling cuts off high-level arterial/venous vessels and redirects flow through the weakly conducing neo-vasculature in the tumor boundary. This leads to locally decreased flow rates, so that drug delivery is an order of magnitude slower. This effect is more pronounced in 2d than in 3d.

5.2 Conclusion

We propose that vessel collapse and local blood flow characteristics have to be correlated via the local shear stress. If the collapse events would occur independently from one another with some probability p, a fundamental law in percolation theory [44] predicts that either the interior of the tumor is completely filled (*i.e.* does not contain large connected necrotic regions) or it is completely void up to a small boundary region —except for one special value for the parameter p, the percolation threshold p_c. We confirmed this scenario by testing different model variants containing uncorrelated collapse events. The existence of a model parameter like the collapse probability that has to be fine-tuned to a special value in order to reproduce vessels that thread the whole tumor would obviously be unsatisfactory. Only if we correlated the vessel collapse with the shear stress, the model predicts a realistic vascular network morphology that is robust against parameter variations. The basic mechanism for this robustness is the redirection of the flow after collapse events into still intact vessels resulting in an increased shear stress in the remaining vessels and thus a drastically reduced collapse probability. Shear stress rather than blood flow as a hemodynamic criterion for vessel stability appears to be plausible, since the endothelial cells in the vessel wall have information about the shear stress but probably less about the total flow. We checked that a correlation of vessel collapses with the blood flow also leads to unrealistic network morphologies in which only a few vessels survive within the whole tumor (*i.e.* a tumor periphery with increased MVD is completely missing). The reason for this is the dependence of the flow from the fourth power of the vessel radius. This leads to a strong variation of the flow between vessels of only slightly different radius, implying the survival of only the thickest vessels if collapse is correlated with the flow.

The emerging tumor vasculature has a complex geometry and a fractal dimension[1] different from the initial arterio-venous network. It has been suggested [38, 39] that the origin of the fractal architecture of tumor vasculature might be based on an underlying invasion percolation process [45, 46] due to inhomogeneities in the growth supporting matrix. Since our theoretical model does not involve any such matrix inhomogeneities, we propose that it is rather the flow-correlated percolation process that determines the fractal properties of the tumor vasculature. A commonly accepted view for a large class of tumors like melanoma [4, 5], also shared by our theoretical approach, is that neo-vascularization mainly occurs at the tumor perimeter and a drastic reduction of vessel density occurs in the interior of the tumor. Within such a scenario it appears unlikely that the fractal properties attained during growth in the periphery, independent of having characteristics of invasion percolation or not, survive the random dilution process in the tumor center.

Our drug flow simulations demonstrated that drug flows relatively well through all of the networks and an infusion time of the order of a few seconds is sufficient to saturate the vasculature with drug. Therefore, without further refinements, the model predicts that drug efficiency is not limited by the transportation process through the vasculature. Considering the model mechanisms which lead to the tumor vasculature, it is plausible that drug reaches (nearly) all parts of the vasculature: Shear force correlate vessel collapse naturally leads to elimination of weakly perfused vessels. In the case of random collapses, pressure

[1] *Fractal dimension* denotes here the number that one obtains by a box-counting procedure and does not intend to imply that the tumor vasculature, neither *in vivo* nor *in silico*, represents a mathematical fractal, or a good physical realization of a mathematical fractal.

gradients are still sufficient to drive blood through the vessels, but an order of magnitude slower.

In [18] it was found that the morphology of tumor vasculature plays a crucial role in drug delivery and that changes to key system parameters could have a big impact on the structure of the vasculature. The origin of this discrepancy with our conclusion lies in the different model assumption: In [18] a strictly avascular tumor was considered, where sprouts migrate towards the tumor, but are not allowed to enter it. These networks exhibit extremely high connectivity close to the tumor surface but the involved angio-adaptation mechanisms lead to vasodilation of comparably few pathways. Depending on the model parameters the number of high-throughput vessels and their distance to the tumor varies sufficiently to lead to uptake rates which vary by several orders of magnitude.

In contrast to this we study here a type of tumor like melanoma, which are primarily vascularized by co-option rather than vessel ingrowth [4,5]. For them, as we have demonstrated, a blood-borne "delivery problem" does not exist. This does however not automatically imply that drug reaches all tumor cells since neither drug transport through the tumor tissue nor drug uptake have been addressed [47]. Regarding tissue transport it is known that the difference between interstitial fluid pressure (IFP) and microvascular pressure (MVP) is low due to vessel leakiness. Since convective transport is driven by pressure differences, high IFP could pose a barrier to drug delivery [48]. On the other hand, leakiness and MVP-IFP gradients could lead to premature release predominantly in locally restricted regions around vessels where blood enters the tumor. Vessels in the outflow regions would thus be depleted of drug. Locally released drug would then be transported by IFP gradients out of the tumor. Furthermore drugs usually consist of large macromolecules. Their low diffusibility through the vessel wall and generally lower diffusibility than oxygen could lead to situations where sufficient oxygen reaches certain TCs to let them remain viable, but not enough drug reaches them to kill them off due to the lower diffusion radius. Thus we conclude that, to a higher degree than the vessels morphology, processes like transportation out of the vessels through convection and diffusion seem to be key factors in successful drug delivery. It is straightforward to include and analyze these mechanisms into the model presented here.

References

1. P. Carmeliet, R.K. Jain, Nature **407**, 249 (2000).
2. J. Holash *et al.*, Science **284**, 1994 (1999).
3. J. Holash, S.J. Wiegand, G.D. Yancopoulos, Oncogene **18**, 5356 (1999).
4. B. Döme, S. Paku, B. Somlai, J. Tímár, J. Path. **197**, 355 (2002).
5. B. Döme, M.J.C. Hendrix, S. Paku, S., J. Tóvári, J. Tímár, J. Path. **170**, 1 (2007).
6. P. Tracqui, Rep. Prog. Phys. **72**, 056701 (2009).
7. J.S. Lowengrub, H.B. Friboes, F. Jin, Y.-L. Chuang, X. Li, P. Macklin, S.M. Wise, V. Cristini, Nonlinearity **23**, R1 (2010).
8. D. Balding, D.L.S. McElwain, J. Theor. Biol. **114**, 53 (1985).
9. M.A.J. Chaplain, A.M. Stuart, IMA J. Math. Appl. Med. Biol. **10**, 149 (1993).
10. M.A.J. Chaplain, S.M. Giles, B.D. Sleeman, R.J. Jarvis, J. Math. Biol. **33**, 744 (1995).
11. H.M. Byrne, M.A.J. Chaplain, Bull. Math. Biol. **57**, 461 (1995).
12. M.J. Holmes, B.D. Sleeman, J. Theor. Biol. **202**, 95 (2000).
13. T. Alarcon, H. Byrne, P. Maini, J. Theor. Biol. **225**, 257 (2003).
14. R. Betteridge, M.R. Owen, H. Byrne, T. Alarcon, P. Maini, Netw. Hetero. Media **1**, 515 (2006).
15. M.R. Owen, T. Alarcon, P. Maini, H. Byrne, J. Math. Biol. **58**, 689 (2008).
16. A.R.A. Anderson, M.A.J. Chaplain, Bull. Math. Biol. **60**, 857 (1998).
17. S.R. McDougall, A.R.A. Anderson, M.A.J. Chaplain, J.A. Sherrat, Bull. Math. Biol. **64**, 673 (2002).
18. S.R. McDougall, A.R.A. Anderson, M.A.J. Chaplain, J. Theor. Biol. **241**, 564 (2006).
19. A. Stephanou, S.R. McDougall, A.R.A. Anderson, M.A.J. Chaplain, Math. Comput. Model. **41**, 1137 (2005).
20. X. Zheng, S.M. Wise, V. Cristini, Bull. Math. Biol. **67**, 211 (2005).
21. H.B. Frieboes, J.S. Lowengrub, S. Wise, X. Zheng, P. Macklin, E. Bearer, V. Cristini, NeuroImage **37**, 59 (2007).
22. S.M. Wise, J.S. Lowengrub, H.B. Frieboes, V. Cristini, J. Theor. Biol. **253**, 524 (2008).
23. P. Macklin, S. McDougall, A.R.A. Anderson, M.J. Chaplain, V. Cristini, J. Lowengrub, J. Math. Biol. **58**, 765 (2008).
24. J. Wu, Q. Long, S.X. Xu, A.R. Padhani, J. Biomech. **42**, 712 (2009).
25. K. Bartha, H. Rieger, J. Theor. Biol. **241**, 903 (2006).
26. D.S. Lee, K. Bartha, H. Rieger, Phys. Rev. Lett. **96**, 058104-1 (2006).
27. M. Welter, K. Bartha, H. Rieger, J. Theor. Biol. **250**, 257 (2008).
28. A. Shirinifard, J.S. Gens, B.L. Zaitlen, N.J. Poplawski, M. Swat, PLoS ONE **4**, e7190 (2009).
29. M. Welter, K. Bartha, H. Rieger, J. Theor. Biol. **259**, 405 (2009).
30. R. Erber *et al.*, EMBO **25**, 628 (2006).
31. K. Bentley, H. Gerhardt, P.A. Bates, J. Theor. Biol. **250**, 25 (2008).
32. H. Gerhardt *et al.*, J. Cell Biol. **161**, 1163 (2003).
33. V. Nehls, R. Herrmann, M. Hünken, Histochem. Cell. Biol. **109**, 319 (1998).
34. S. Dimmeler, A.M. Zeiher, Circ. Res. **87**, 434 (2000).
35. R. Gödde, H. Kurz, Dev. Dyn. **220**, 387 (2001).
36. P. Vajkoczy, M.D. Menger, J. Neurooncol. **50**, 99 (2000).
37. A.R. Pries, T.W. Secomb, T. Gessner, M.B. Sperandio, J.F. Gross, P. Gaehtgens, Circ. Res. **75**, 904 (1994).
38. J.W. Baish, R.K. Jain, R.K., Cancer Res. **60**, 3683 (2000).
39. Y. Gazit, D.A. Berk, L.T.B. Michael Leunig, R.K. Jain, Phys. Rev. Lett. **75**, 2428 (1995).
40. J.W. Baish, R.K. Jain, Nat. Med. **4**, 984 (1998).
41. H.-W. Chung, H.-J. Chung, Cancer Res. **61**, 8347 (2001).
42. R. Paul, Eur. Phys. J. E **30**, 101 (2009).
43. S. Pahernik, J. Griebel, A. Botzlar, T. Gneiting, M. Brandl, M. Dellian, A.E. Goetz, Brit. J. Canc. **85**, 1655 (2001).

44. D. Stauffer, A. Aharony, *Introduction to Percolation Theory*, 2nd edition (Taylor & Francis, London, 1992).
45. L. Furuberg, J. Feder, A. Aharony, T. Jossang, Phys. Rev. Lett. **61**, 2117 (1988).
46. A.P. Sheppard, M.A. Knackstedt, W.V. Pinczewski, M. Sahimi, J. Phys. A **32**, L521 (1999).
47. A.I. Minchinton, I.F. Tannock, Nat. Rev. Canc. **6**, 583 (2006).
48. Y. Hassid, E. Furman-Haran, R. Margalit, R. Eilam, H. Degani, Cancer Res. **66**, 4159 (2006).